

High-resolution Mn *K*-edge x-ray emission and absorption spectroscopy study of the electronic and local structure of the three different phases in $\text{Nd}_{0.5}\text{Sr}_{0.5}\text{MnO}_3$

S. Lafuerza,^{1,*} J. García,² G. Subías,² J. Blasco,² and P. Glatzel¹¹*ESRF-The European Synchrotron, 71, Avenue des Martyrs, Grenoble, France*²*Instituto de Ciencia de Materiales de Aragón, Departamento de Física de la Materia Condensada,**CSIC-Universidad de Zaragoza, C/ Pedro Cerbuna 12, 50009 Zaragoza, Spain*

(Received 4 March 2016; revised manuscript received 11 April 2016; published 9 May 2016)

$\text{Nd}_{0.5}\text{Sr}_{0.5}\text{MnO}_3$ is particularly representative of mixed-valent manganites since their three characteristic macroscopic phases (charge-ordered insulator, ferromagnetic-metallic, and paramagnetic insulator) appear at different temperatures. We here report a complete x-ray emission and absorption spectroscopy (XES-XAS) study of $\text{Nd}_{0.5}\text{Sr}_{0.5}\text{MnO}_3$ as a function of temperature to investigate the electronic and local structure changes of the Mn atom in these three phases. Compared with the differences in the XES-XAS spectra between $\text{Nd}_{0.5}\text{Sr}_{0.5}\text{MnO}_3$ and the single-valent reference compounds NdMnO_3 (Mn^{3+}) and Sr/CaMnO_3 (Mn^{4+}), only modest changes have been obtained across the magnetoelectrical transitions. The XES spectra, including both the Mn $K\alpha$ and $K\beta$ emission lines, have mainly shown a subtle decrease in the local spin density accompanying the passage to the ferromagnetic-metallic phase. For the same phase, the small intensity variations in the pre-edge region of the high-resolution XAS spectra reflect an increase of the p - d mixing. The analysis of these XAS spectra imply a charge segregation between the two different Mn sites far from one electron, being in intermediate valences $\text{Mn}^{+3.5\pm\delta/2}$ ($\delta < 0.2 e^-$) for all the phases. Our results indicate that the spin, charge, and geometrical structure of the Mn atom hardly change among the three macroscopic phases demonstrating the strong competition between the ferromagnetic conductor and the charge-ordered insulator behaviors in the manganites.

DOI: [10.1103/PhysRevB.93.205108](https://doi.org/10.1103/PhysRevB.93.205108)

I. INTRODUCTION

Mixed-valent manganese perovskites of the type $\text{RE}_{1-x}\text{A}_x\text{MnO}_3$, $\text{RE}_{1-x}\text{A}_{1+x}\text{MnO}_4$, and $\text{RE}_{2-2x}\text{A}_{1+2x}\text{Mn}_2\text{O}_7$ (RE = rare-earth, A = alkaline-earth), hereafter referred to as manganites, have recently been the subject of an extensive and deep study due to the occurrence of exotic phenomena like colossal magnetoresistance or so-called charge ordering (CO) [1–4]. Despite this broad interest, a complete and comprehensive understanding of the changes in the Mn local electronic structure along with the complex behavior exhibited by these manganites is lacking. Depending on the formal valence state of the Mn atom, they show different magnetic and electrical phases (including ferromagnetic-metal or antiferromagnetic-insulator) and also phases identified as charge-orbital ordered. The classical description of this behavior in terms of ionic $\text{Mn}^{3+}/\text{Mn}^{4+}$ configurations which includes the double exchange mechanism has been challenged by both experimental results and electronic structure calculations [5–11].

Among them, half-doped manganites with general formula $(\text{RE}_{0.5}\text{A}_{0.5})\text{MnO}_3$ present many intriguing features such as real space ordering of charge, spontaneous phase separation, field-induced antiferromagnetic-insulating to ferromagnetic-metallic transition resulting in a giant change in resistivity, etc. [4] CO of $\text{Mn}^{3+}/\text{Mn}^{4+}$ and orbital ordering was proposed as the fingerprint of the charge exchange antiferromagnetic-insulating low temperature phase [12–20]. The conventional model used to describe this low-temperature phase is a one-dimensional zigzag chain of Mn atoms in the ab plane coupled antiferromagnetically to each other with a checkerboard ordering of the Jahn-Teller distorted Mn^{3+} and isotropic Mn^{4+}

ions. In particular, $\text{Nd}_{0.5}\text{Sr}_{0.5}\text{MnO}_3$ is very representative since the three macroscopic phases of half-doped manganites (charge ordered insulator, ferromagnetic conductor, and paramagnetic insulator) appear at different temperatures [21]. Above the ferromagnetic ordering temperature $T_C = 255$ K it is a paramagnetic insulator, in the range $255 \text{ K} \geq T \geq 150 \text{ K}$ it is a magnetoresistive ferromagnetic metal, and below the antiferromagnetic ordering temperature $T_N = 150$ K it shows CO. In short, the proposed mechanism of the phase transitions has been explained as follows: In the paramagnetic phase, the doped holes are randomly localized at the Mn sites being the fluctuation time among the sites larger than the permanence time at each site. Then the ferromagnetic-metal phase is assumed to appear due to the double exchange mechanism and the doped holes are highly delocalized and spread out over the Mn atoms. Finally, the insulator CO phase is described as the spatial localization of the doped holes with a periodic ordering of Mn^{3+} and Mn^{4+} ions.

X-ray absorption measurements at the Mn *K* edge in the $\text{La}_{1-x}\text{Ca}_x\text{MnO}_3$ series have demonstrated the absence of integer ionic states of the Mn atoms [6,8,9,22–25]. In addition, results of resonant x-ray scattering (RXS) at the Mn *K* edge in half-doped manganites have shown that the electronic disproportionation between the different sites in the checkerboard Mn ordering is of the order of 0.2 electrons [5,26–30]. On the other hand, extended x-ray absorption fine structure (EXAFS) data in $\text{La}_{1-x}(\text{Ca},\text{Sr})_x\text{MnO}_3$ compounds have proven that the local structure around the Mn atom is distorted in both the charge-ordered and paramagnetic phases, whereas the ferromagnetic-metallic phase appears concomitantly with a collapse of this distribution into a symmetric environment of the nearest-neighboring O atoms [6,31–33].

We here present a complete study of the local electronic and geometrical structure of the Mn atom in the three different

*sara.lafuerza@esrf.fr

phases of $\text{Nd}_{0.5}\text{Sr}_{0.5}\text{MnO}_3$ by high-resolution x-ray emission and absorption spectroscopy (XES-XAS) [34–37]. The detection of the emitted x-rays after K edge photon absorption as a function of both incident and emitted energies makes the high-resolution XES-XAS techniques unique to detect small electronic and/or geometrical differences among the different phases. Like XAS, XES is also sensitive to the oxidation state of the Mn atoms but it has the advantage that it is less dependent on the ligand environment. We have recorded XES at both the Mn $K\alpha$ and $K\beta$ lines. The $K\alpha$ lines are the strongest fluorescence lines and arise from $2p \rightarrow 1s$ transitions; while about 8 times weaker are the core-to-core (CTC) $K\beta$ lines, which result from $3p \rightarrow 1s$ transitions; and again 50–100 times weaker are the valence-to-core (VTC) $K\beta$ lines which are transitions from the valence shell to the $1s$ state [35]. We also performed high-energy resolution fluorescence-detected (HERFD) absorption spectroscopy by setting the emission energy to the maxima of the main fluorescence lines and recording the intensity as a function of the energy of the incident photons across the Mn K edge. For the sake of comparison, the same measurements were carried out in parallel on the related single-valent compounds: NdMnO_3 (Mn^{3+}), SrMnO_3 (Mn^{4+}), and CaMnO_3 (Mn^{4+}). NdMnO_3 and CaMnO_3 undergo antiferromagnetic transitions at a T_N of about 78 K [38] and 125 K [39], respectively, whereas cubic SrMnO_3 adopts an antiferromagnetic structure between 230 and 260 K depending on the oxygen stoichiometry of the samples [40–41].

We note that because of the interference between the Mn K edge and the Nd L_2 edge, for $\text{Nd}_{0.5}\text{Sr}_{0.5}\text{MnO}_3$ the EXAFS signal cannot be obtained by means of standard XAS. Interestingly, we have been able to work out the EXAFS spectra of this compound by using the simultaneously recorded total fluorescence and high-resolution data measured at the maximum of the $K\alpha_1$ emission line. In this way, the temperature dependence of the EXAFS signal across the three different phases of $\text{Nd}_{0.5}\text{Sr}_{0.5}\text{MnO}_3$ has also been characterized.

Our results show that the electronic state of the Mn atom in $\text{Nd}_{0.5}\text{Sr}_{0.5}\text{MnO}_3$ is intermediate between the single-valent compounds and changes very little in the three phases: paramagnetic-insulator, ferromagnetic-metal, and antiferromagnetic charge-ordered. The similarity of the Mn electronic and local structural state at the different magnetoelectrical phases explains the strong competition between the ferromagnetic-metallic and the CO phases in this compound and by extension in the manganites.

II. EXPERIMENTAL

Polycrystalline samples of $\text{Nd}_{0.5}\text{Sr}_{0.5}\text{MnO}_3$, NdMnO_3 , SrMnO_3 , and CaMnO_3 were synthesized using a sol-gel method by the citrate route. Details about the synthesis are given in Refs. [42,43]. The obtained specimens were single phase as confirmed by conventional x-ray powder diffraction. Magnetic measurements were also performed between 5 and 300 K using a commercial superconducting quantum interference device (SQUID) magnetometer. According to the magnetic susceptibility measurements, $\text{Nd}_{0.5}\text{Sr}_{0.5}\text{MnO}_3$ shows two phase transitions at $T_C \approx 255$ K and at $T_N \approx 150$ K [5].

The experiment was performed at ID26 beamline of the European Synchrotron Radiation Facility (ESRF) in Grenoble

(France). The incident energy was tuned through the Mn K edge by means of a pair of cryogenically cooled Si(311) monochromator crystals. Rejection of higher harmonics was achieved by three Si mirrors working under total reflection (2.5 mrad). A reference Mn metallic foil was used to calibrate the monochromator energy by setting the first inflection point of the Mn K edge at 6539 eV. The inelastically scattered photons were analyzed using a set of four spherically bent Ge(333) and Ge(440) crystals for the Mn $K\alpha$ and $K\beta$ lines, respectively. The analyzer crystals were arranged with the sample and detector (avalanche photodiode) in a vertical Rowland geometry ($R \approx 1$ m). The total experimental broadening, determined as the average of the full width at half maximum (FWHM) of the elastic profiles, was about 0.4 eV (Mn $K\alpha$) and 0.7 eV (Mn $K\beta$). Nonresonant Mn $K\alpha$ and $K\beta$ XES scans were recorded at incident energy of 6700 eV. HERFD-XAS spectra at the Mn K edge were measured at various emission energies while recording simultaneously the total fluorescence yield (TFY) with a diode. X-ray absorption near edge structure (XANES) spectra were collected for all the samples at the maximum of the Mn $K\alpha_1$ emission line while EXAFS spectra were only measured in $\text{Nd}_{0.5}\text{Sr}_{0.5}\text{MnO}_3$. Spin-selective XANES spectra were measured at the maximum of the Mn $K\beta_{1,3}$ emission line for each sample and also at the maximum of the Mn $K\beta'$ shoulder. A continuous He-flow cryostat was used for the temperature-dependent measurements. The data were collected on concentrated pellets after finding no difference in the XANES spectra as compared with 5 – 10% in mass diluted pellets. Self-absorption effects can be discarded as almost no difference is found between XANES spectra recorded in TFY mode and those measured in transmission mode with optimal thickness to get a jump at the edge of about 1.

The applied data treatment procedures are described in the following. The XES spectra have been normalized with respect to the area using the range 5876–5908 eV for the Mn $K\alpha$ XES and the range 6461–6506 eV for the Mn $K\beta$ XES. The Mn $K\alpha$ XES spectra have been fitted with two Lorentzian functions to determine the FWHM of the $K\alpha_1$ line [44]. The Mn $K\beta$ VTC region spectra have been further treated by performing a background subtraction in order to get rid of the contribution from the CTC main line tail. For that, we have modelled the background using seven Voigt functions that have been fitted to several data points below (6492–6515 eV) and above (6540–6565 eV) the VTC features following the procedure described in Ref. [45]. Regarding the x-ray absorption data, the XANES spectra have been normalized to the high-energy part well above the absorption edge (about 100 eV) [46]. The Fourier transforms (FTs) of the EXAFS signals were calculated for a k range of $1.5\text{--}12 \text{ \AA}^{-1}$ using a sine window. The EXAFS structural analysis has been performed using theoretical phases and amplitudes calculated by the FEFF-6 code [47] and fits to the experimental data were carried out in R space with the ARTEMIS programme of the Demeter package [48].

III. RESULTS

A. Mn $K\alpha$ and $K\beta$ XES spectra

Figure 1 compares the Mn $K\alpha$ XES spectra of $\text{Nd}_{0.5}\text{Sr}_{0.5}\text{MnO}_3$, NdMnO_3 (Mn^{3+}), SrMnO_3 (Mn^{4+}), and

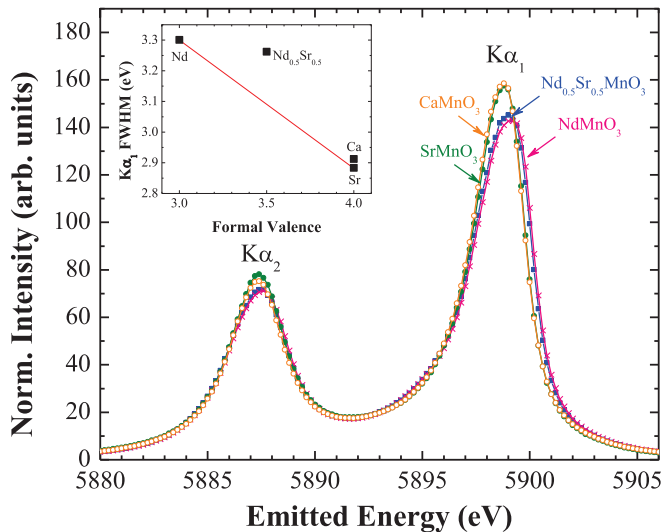


FIG. 1. Normalized Mn $K\alpha$ XES spectra of $\text{Nd}_{0.5}\text{Sr}_{0.5}\text{MnO}_3$, NdMnO_3 , SrMnO_3 , and CaMnO_3 measured at 80 K. Inset: $K\alpha_1$ line full width at half maximum (FWHM) from the same data as a function of formal valence. The red line is a linear fit considering only NdMnO_3 and SrMnO_3 .

CaMnO_3 (Mn^{4+}) measured at 80 K. These spectra consist of two peaks, $K\alpha_1$ and $K\alpha_2$, which correspond to $2p_{3/2}$ and $2p_{1/2}$ final states, respectively. We note that the maximum of the $K\alpha_1$ peak is shifted to higher energies by about 0.2 eV for the Mn^{3+} compound compared to the Mn^{4+} samples while the spectrum of mixed-valent $\text{Nd}_{0.5}\text{Sr}_{0.5}\text{MnO}_3$ lies closer to that of NdMnO_3 . Clearly, the $K\alpha$ XES of $\text{Nd}_{0.5}\text{Sr}_{0.5}\text{MnO}_3$ cannot be described by a 1:1 superposition of the spectra of NdMnO_3 and SrMnO_3 . We have fitted the spectrum using the formula $\sigma_{\text{Nd}_{0.5}\text{Sr}_{0.5}\text{MnO}_3} = (1-x)\sigma_{\text{NdMnO}_3} + x\sigma_{\text{SrMnO}_3}$ and we have found the best fit for the addition $0.8\sigma_{\text{NdMnO}_3} + 0.2\sigma_{\text{SrMnO}_3}$. Therefore, the weight needed in the spectra is not simply equal to the doping concentration. As reported in previous works [35,44,49], the $K\alpha_1$ FWHM can be related to the spin state. The inset of Fig. 1 shows the evolution of the $K\alpha_1$ line FWHM for the four compounds plotted versus formal valence. We note that the value corresponding to $\text{Nd}_{0.5}\text{Sr}_{0.5}\text{MnO}_3$ falls out from the linear dependence between these two parameters considering the single-valent compounds and appears nearer to the one of NdMnO_3 .

We continue with the Mn CTC $K\beta$ XES spectra of the same samples measured at room temperature (RT), which are shown in Fig. 2. In this case, the spectral features arise from a $3p \rightarrow 1s$ decay process and are separated into the strong $K\beta_{1,3}$ peak and a broad $K\beta'$ shoulder at lower emitted energy. The presence of the $K\beta'$ satellite and the energy splitting between the $K\beta_{1,3}$ and $K\beta'$ lines are determined by the intra-atomic exchange interaction between the spin of the $3p$ hole and the $3d$ electrons. The strong $K\beta_{1,3}$ peak (low intense $K\beta'$ shoulder) is mainly arising from the coupling between the $3p$ hole, which is antiparallel (parallel) to the total spin of the $3d$ electrons. In this way, compounds with the same spin state show very similar spectra as observed for our samples with formal Mn^{4+} ($3d^3$) ionic states. Nevertheless, systematic changes with Mn valence when increasing from 3+ to 4+ are observed. The Mn valence

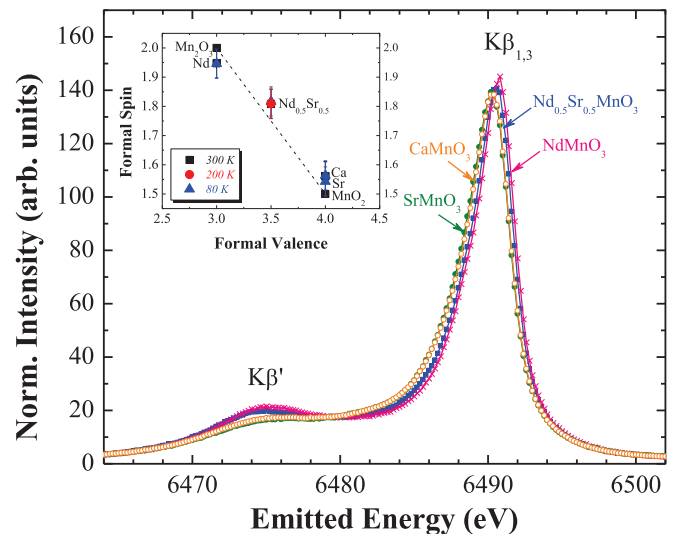


FIG. 2. Normalized Mn CTC $K\beta$ XES spectra of $\text{Nd}_{0.5}\text{Sr}_{0.5}\text{MnO}_3$, NdMnO_3 , SrMnO_3 , and CaMnO_3 measured at RT. Inset: Formal spin values derived from the IAD analysis of the same data as described in the text plotted versus formal valence. Error bars have been estimated by comparison with the data points of the two binary oxides and the solid line is the linear dependence considering the latter points.

increase is reflected in the shift of the $K\beta_{1,3}$ maximum to lower energy (~ 0.4 eV) and strong broadening on its low-energy side, and the intensity loss of the $K\beta'$ shoulder. On the other hand, the spectrum of $\text{Nd}_{0.5}\text{Sr}_{0.5}\text{MnO}_3$ lies in between the Mn^{3+} and Mn^{4+} groups but closer to the spectrum of the Mn^{3+} sample as found in the $K\alpha$ XES spectra. In this case, the best agreement is found for the addition $0.7\sigma_{\text{NdMnO}_3} + 0.3\sigma_{\text{SrMnO}_3}$. Tyson *et al.* [8] also reported a nonlinear dependence between the mix weights and the doping concentration in the Mn CTC $K\beta$ XES data of the related system $\text{La}_{1-x}\text{Ca}_x\text{MnO}_3$ for $x < 0.4$, being the weights for $x = 0.3$ such that $0.9\sigma_{\text{LaMnO}_3} + 0.1\sigma_{\text{CaMnO}_3}$. Besides, we have analyzed the Mn CTC $K\beta$ XES spectra using the integrated absolute difference (IAD) method [49] in order to retrieve the evolution of the Mn local spin moment both across the different compounds and as a function of temperature. This method allows quantitatively obtaining the relative change in the local $3d$ spin magnetic moment by integrating the absolute value of the difference between sample spectrum and a reference spectrum. In this analysis, we have also included the data of the binary oxides Mn_2O_3 (Mn^{3+}) and MnO_2 (Mn^{4+}) and the latter compound has been used as reference. In order to obtain a linear relationship between IAD and spin (S), we have assumed an ionic picture for MnO_2 and Mn_2O_3 and used their formal spin values which are $S = 3/2$ and $S = 2$, respectively since Mn is in high-spin configuration. The inset of Fig. 2 shows the formal spin obtained in this way plotted versus formal valence for all the compounds. The formal spin state of Mn in $\text{Nd}_{0.5}\text{Sr}_{0.5}\text{MnO}_3$ is intermediate between the single-valent samples but it deviates from the corresponding average spin state in agreement with the 0.7:0.3 ratio for the $\text{NdMnO}_3/\text{SrMnO}_3$ weights previously obtained.

In Fig. 3 are shown the spectra of $\text{Nd}_{0.5}\text{Sr}_{0.5}\text{MnO}_3$ measured at temperatures corresponding to the three phases (300 K,

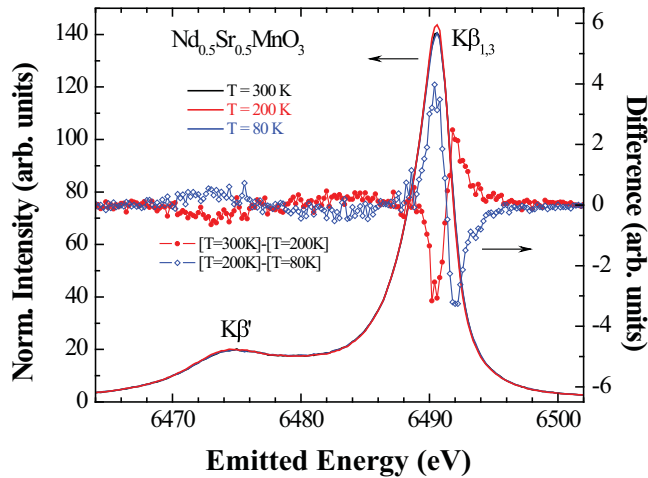


FIG. 3. Comparison between the normalized Mn CTC $K\beta$ XES spectra of $\text{Nd}_{0.5}\text{Sr}_{0.5}\text{MnO}_3$ measured at 300 K, 200 K, and 80 K (left axis) and differences between the same spectra (right axis).

200 K, and 80 K). Despite the significant changes in the macroscopic properties, these spectra are almost identical (see also the corresponding IAD values in the inset of Fig. 2), indicating that the electronic states at the Mn atom are very similar for the three different phases. The difference spectra of $\text{Nd}_{0.5}\text{Sr}_{0.5}\text{MnO}_3$ formed by subtracting the data at two temperatures are also displayed. The differences $[T = 300 \text{ K}] - [T = 200 \text{ K}]$ and $[T = 200 \text{ K}] - [T = 80 \text{ K}]$ reflect the changes that take place when entering the ferromagnetic-metallic and antiferromagnetic charge-ordered phases, respectively. We find small but clearly perceptible changes and the signs of the difference signals are reversed. No changes are observed in the difference $[T = 300 \text{ K}] - [T = 80 \text{ K}]$ and the spectra of NdMnO_3 , SrMnO_3 , and CaMnO_3 measured at 80 K are also alike the data at 300 K (not shown). Similarly to Qian *et al.* [50] and Herrero-Martín *et al.* [51], we have also evaluated the difference signal resulting from a change in the Mn formal valence state by doing $\sigma_{\text{Sr/CaMnO}_3} - \sigma_{\text{NdMnO}_3}$, $\sigma_{\text{Nd}_{0.5}\text{Sr}_{0.5}\text{MnO}_3} - \sigma_{\text{NdMnO}_3}$, and $\sigma_{\text{Mn}_2\text{O}_3} - \sigma_{\text{Mn}_2\text{O}_3}$. However, the spectral changes induced by a Mn formal valence increase do not resemble those in the differences $[T = 300 \text{ K}] - [T = 200 \text{ K}]$ and $[T = 200 \text{ K}] - [T = 80 \text{ K}]$. The observed thermal behavior could thus be interpreted as a change in the local spin density between the ferromagnetic phase and the paramagnetic and antiferromagnetic phases. In order to discern whether this change corresponds to either an increase or decrease of the local spin density, we have computed the first moment ($\langle E \rangle = \sum_j (E_j I_j) / \sum_j I_j$) of the $K\beta_{1,3}$ peak in the spectra at the different temperatures using the area 6485–6495 eV. While this method is less robust to detect small changes than the IAD values, it has the advantage that it maintains the sign of the shift (which is lost in the IAD analysis). We obtain $\langle E \rangle$ equal to 6489.81 and 6489.82 eV for 300 K and 80 K, respectively, and $\langle E \rangle = 6489.80$ eV for 200 K. Since the spin state and the first moment of the $K\beta_{1,3}$ peak shift in a linear fashion as shown previously for other Mn compounds [35], we can then conclude that our Mn CTC $K\beta$ XES spectra of $\text{Nd}_{0.5}\text{Sr}_{0.5}\text{MnO}_3$ as a function of temperature reflect a subtle decrease of the local spin density in the ferromagnetic-metallic phase as expected from the charge delocalization.

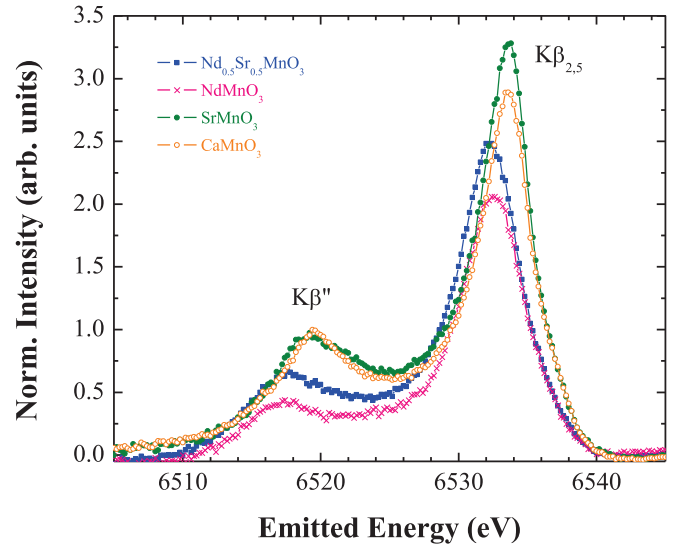


FIG. 4. Normalized Mn VTC $K\beta$ XES spectra of $\text{Nd}_{0.5}\text{Sr}_{0.5}\text{MnO}_3$, NdMnO_3 , SrMnO_3 , and CaMnO_3 measured at RT after background removal.

While the CTC $K\beta$ emission lines are sensitive to the local magnetic moment, VTC $K\beta$ emission lines mainly probe the occupied metal p -density of states (DOS) up to 25 eV below the Fermi energy. The x-ray emission process is dominated by dipole transitions and therefore the spectral features correspond to valence band states with metal p symmetry. Since the metal p -DOS is strongly mixed with ligand orbitals, the intensities of the two observed features, $K\beta''$ shoulder and $K\beta_{2,5}$ line, reflect the amount of hybridization between the metal p occupied electronic levels and ligand s and p orbitals, respectively [45]. Figure 4 shows the VTC $K\beta$ XES spectra of all the samples taken at RT after background removal. The compounds with higher Mn formal valence state, Sr/CaMnO_3 , show the strongest $K\beta''$ and $K\beta_{2,5}$ features, indicating a larger hybridization as expected from the shorter Mn-O distance (the average Mn-O distance is 2.05 Å for NdMnO_3 [52] while for Sr/CaMnO_3 is 1.90 Å [31,53,54], in agreement with a larger ionic radii for Mn^{3+} compared with Mn^{4+}). As occurred in the case of the Mn $K\alpha$ and CTC $K\beta$ emission lines, the spectrum of $\text{Nd}_{0.5}\text{Sr}_{0.5}\text{MnO}_3$ is very similar to that of NdMnO_3 , even though in this case the $K\beta_{2,5}$ maximum appears slightly shifted to lower energy contrary to the expected position from its oxidation state. A shift of 1 eV is observed between NdMnO_3 and Sr/CaMnO_3 , consistent with the difference in one oxidation state unit [55]. We also measured the VTC $K\beta$ XES spectra at temperatures corresponding to the three phases in $\text{Nd}_{0.5}\text{Sr}_{0.5}\text{MnO}_3$ and at 80 K for the other compounds. However, the spectra do not change with temperature outside the experimental error for any of the samples (not shown).

The main conclusion from the Mn $K\alpha$ and $K\beta$ XES measurements is that while significant changes in the electronic structure are observed between the different reference compounds, only very small variations are detected for $\text{Nd}_{0.5}\text{Sr}_{0.5}\text{MnO}_3$ as a function of temperature despite the different physical properties. The electronic state of the Mn atom seems to be similar in all phases and cannot be described

in terms of a 1:1 superposition of $\text{Mn}^{3+}/\text{Mn}^{4+}$ (neither temporally nor spatially), in agreement with the homogenous mixed-valent character of $\text{Nd}_{0.5}\text{Sr}_{0.5}\text{MnO}_3$. In general, for all the emission spectra, $\text{Nd}_{0.5}\text{Sr}_{0.5}\text{MnO}_3$ shows a behavior closer to NdMnO_3 (Mn^{3+}) than to Sr/CaMnO_3 (Mn^{4+}). However, we find very small temperature changes in the XES spectra of $\text{Nd}_{0.5}\text{Sr}_{0.5}\text{MnO}_3$ accompanying the transition to the ferromagnetic-metallic phase that are interpreted as a decrease in the local spin density and are almost completely reversed when passing to the low-temperature charge-ordered insulating state.

B. High-resolution and spin-selective XANES spectra

Figure 5(a) shows the comparison between the TFY-XANES and the HERFD-XANES spectra measured at the maximum of the $K\alpha_1$ line for the $\text{Nd}_{0.5}\text{Sr}_{0.5}\text{MnO}_3$ sample at RT. The HERFD-XANES shows sharper spectral features (at both the pre-edge structure and white line) than the TFY-XANES. In Fig. 5(b) the HERFD-XANES spectra at the $K\alpha_1$ line are shown for all the compounds. The spectra are shifted following the expected trend with the formal valence state of the Mn atom [56]. The absorption edge appears at a higher energy for the Mn^{4+} compounds (Sr/CaMnO_3) and at a lower energy for NdMnO_3 (Mn^{3+}). The energy separation, also referred to as a chemical shift, is about 3.1 eV as deduced from the maximum of the derivatives of the NdMnO_3 and SrMnO_3 spectra. For $\text{Nd}_{0.5}\text{Sr}_{0.5}\text{MnO}_3$, the absorption edge position lies in between the two extremes suggesting an intermediate valence. The pre-edge structure also evolves in spectral shape and intensity between the samples [see Fig. 5(b), inset]. The pre-edge of Sr/CaMnO_3 exhibits three features: a strong peak at 6542 eV (a2), a weaker shoulder around 2 eV below (a1) and a third peak about 2 eV above (a3). For both NdMnO_3 and $\text{Nd}_{0.5}\text{Sr}_{0.5}\text{MnO}_3$ the pre-edge shows two resolved peaks a1 and a2 of comparable intensities that are shifted to lower energies relative to those in Sr/CaMnO_3 .

Spin-selected x-ray absorption spectroscopy stems from the assumption that the $K\beta$ ($3p \rightarrow 1s$) x-ray emission spectrum can be separated into two internally referenced spin-up and spin-down parts [34,57–59]. The spin-up and spin-down contributions refer to a parallel and antiparallel alignment respectively of the $3p$ hole spin and the local $3d$ moment. One can achieve a local spin selectivity in the K edge absorption spectra by setting the emission energy to either the $K\beta_{1,3}$ main line to get the spin-down contribution, or the $K\beta'$ satellite to obtain the spin-up contribution, and measure the emitted photons as a function of the incident x-ray energy. Figure 5(c) shows the spin-selective XANES spectra measured at the $K\beta_{1,3}$ (spin-down) and $K\beta'$ (spin-up) lines for $\text{Nd}_{0.5}\text{Sr}_{0.5}\text{MnO}_3$ at RT. The XANES at the $K\beta'$ line is shifted to lower energy by about 0.8 eV with respect to the spectrum measured at the $K\beta_{1,3}$ line as deduced from the maximum of the derivatives. Similar results were found for the other samples measured (not shown). Moreover, the prepeaks in the spin-selective XANES at the $K\beta_{1,3}$ and $K\beta'$ lines show the same shift in analogy with previous works in related manganese perovskites [58,60,61].

HERFD-XANES spectra of the different compounds were also measured as a function of temperature. The detailed temperature dependence of the HERFD-XANES spectra was

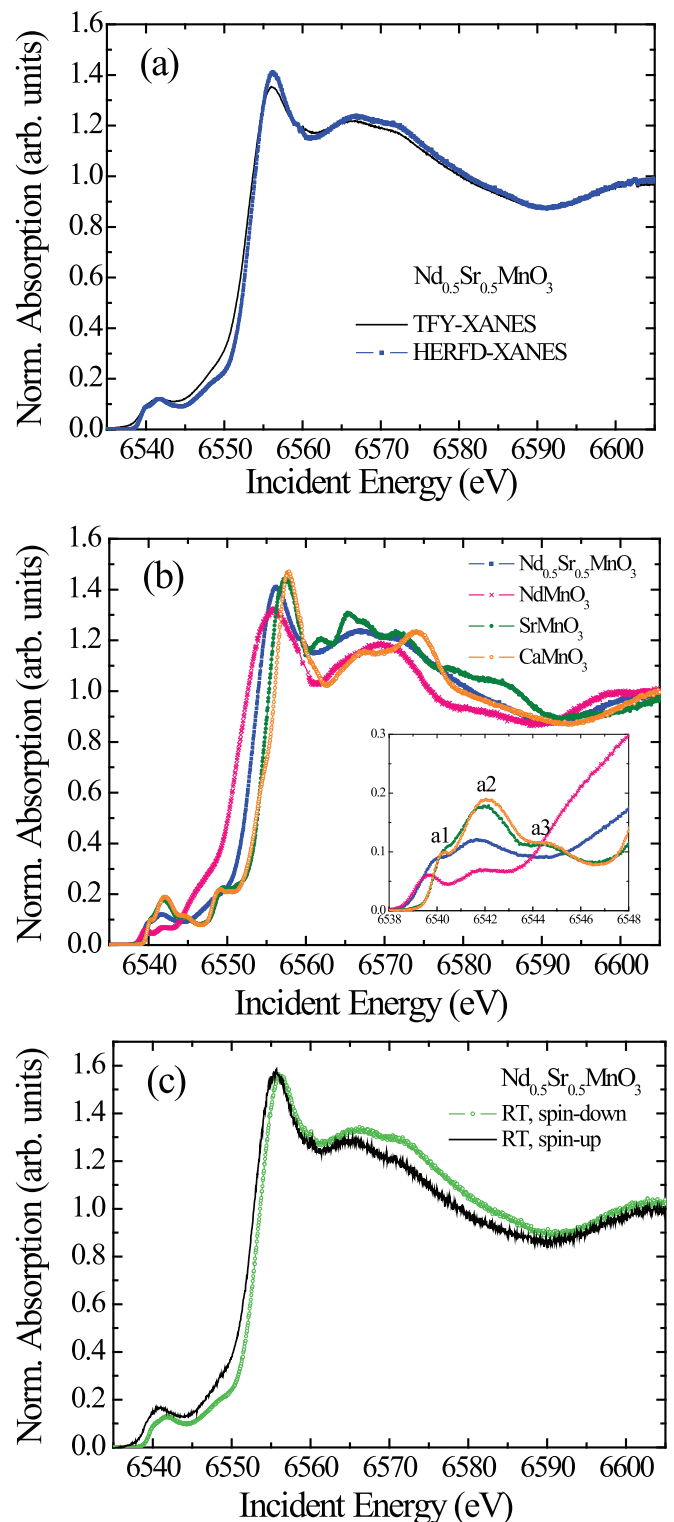


FIG. 5. Normalized XANES spectra at the Mn K edge measured at RT. (a) Comparison between the HERFD-XANES at the $K\alpha_1$ line and TFY-XANES of $\text{Nd}_{0.5}\text{Sr}_{0.5}\text{MnO}_3$. (b) HERFD-XANES at the $K\alpha_1$ line of $\text{Nd}_{0.5}\text{Sr}_{0.5}\text{MnO}_3$, NdMnO_3 , SrMnO_3 , and CaMnO_3 . The inset shows an expansion of the pre-edge region. (c) Spin-selective XANES spectra measured at the Mn $K\beta_{1,3}$ (spin-down) and $K\beta'$ (spin-up) lines for $\text{Nd}_{0.5}\text{Sr}_{0.5}\text{MnO}_3$.

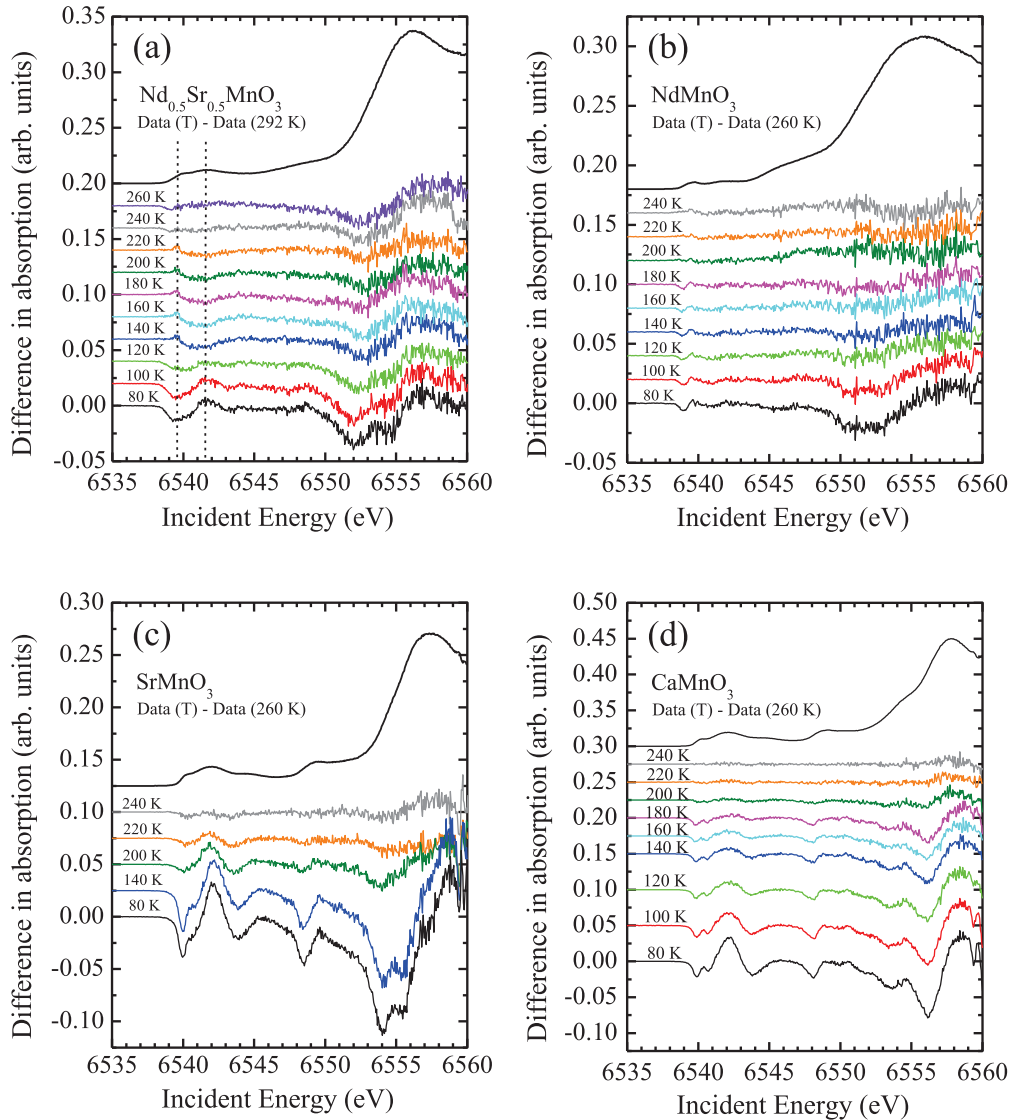


FIG. 6. Difference HERFD-XANES data measured at the Mn $K\alpha_1$ line for (a) $\text{Nd}_{0.5}\text{Sr}_{0.5}\text{MnO}_3$ between 292 K and each T, (b) NdMnO_3 between 260 K and each T, (c) SrMnO_3 between 260 K and each T, and (d) CaMnO_3 between 260 K and each T.

followed between 292 K and 80 K ($\Delta T \approx 20$ K) at the $K\alpha_1$ emission line energy because of the larger intensity of the $K\alpha_1$ line and the consequently higher signal-to-noise ratio. The difference signal obtained by subtracting the HERFD-XANES data at the highest temperature from all the data files (at different temperatures upon cooling down) has been evaluated to better elucidate the possible changes. Figure 6 shows the difference signals obtained for $\text{Nd}_{0.5}\text{Sr}_{0.5}\text{MnO}_3$, NdMnO_3 , SrMnO_3 , and CaMnO_3 . The main changes occur at the prepeaks and rising edge. Regarding the evolution at the main edge, an increase of the slope is observed when cooling down. This effect is common for all the samples and can be explained as due to the freezing of the thermal vibrations [62,63]. We note that the weaker variation occurs for NdMnO_3 where the Mn atom is surrounded by a tetragonal-distorted oxygen octahedron which implies a less sharp rising edge and thus obscures the thermal vibrations. Concerning the prepeaks, NdMnO_3 , SrMnO_3 , and CaMnO_3 exhibit a monotonic evolution with decreasing temperature, whereas in

$\text{Nd}_{0.5}\text{Sr}_{0.5}\text{MnO}_3$ the structures in the difference signal show a change of sign. An upward peak appears at 6540 eV below 240 K when the paramagnetic-insulator to ferromagnetic-metallic transition occurs that becomes downward below 140 K, which corresponds to the insulating charge-ordered low temperature phase. Conversely, a downward peak occurs at 6542 eV ($T < 240$ K) that becomes upward below 140 K. This result suggests that the p - d hybridization increases in the ferromagnetic-metallic phase and decreases in the insulating phase. The hybridization increase in the ferromagnetic phase is consistent with the reduction in local spin moment derived from the Mn CTC $K\beta$ XES spectra.

C. EXAFS spectra

The EXAFS signal at the Mn K edge of $\text{Nd}_{0.5}\text{Sr}_{0.5}\text{MnO}_3$ cannot be obtained with a sufficiently long range in k for quantitative analysis by conventional XAS measurements due to interference with the Nd L_2 edge (6722 eV). We have

overcome this problem by combining the HERFD-EXAFS at the Mn $K\alpha_1$ line with the simultaneously measured TFY-EXAFS. We note that these EXAFS spectra suffer from Nd self-absorption at the L_2 edge energy which appears as a positive contribution in the TFY and as a negative contribution in the HERFD as discussed by Bianchini *et al.* [64]. In Fig. 7(a) we show that the EXAFS signal free of Nd self-absorption can be obtained from the weighted addition of the HERFD and TFY spectra. The weight of each spectrum is fitted to suppress the intense Nd L_2 white line. In any case, the EXAFS signal free of Nd self-absorption does not significantly change for a variation of 5% of the weighted addition.

The thus obtained EXAFS signals and the corresponding FTs are shown as a function of temperature in Figs. 7(b) and 7(c), respectively. We observe a weak thermal dependence of the EXAFS signal. The spectra were fitted including the first (O atoms) and second shell contributions (Nd and Sr atoms). The analysis shows that the Mn atom is surrounded by six O atoms at the same distance, i.e., nearly a regular octahedron, with a relatively high Debye-Waller (D-W) factor at 292 K. The Mn-O distance hardly changes with temperature showing simply a small increase at the onset of the ferromagnetic-metallic phase, where it is also observed a minimum in the D-W factor indicating a less distorted octahedron [see inset of Fig. 7(c)]. These results show that the interatomic distance does not follow a normal expansion but remains nearly constant. On the other hand, the Debye-Waller factor does not follow a standard thermal variation (Debye or Einstein models) and the high value at low temperatures manifests a small structural distortion.

IV. DISCUSSION AND CONCLUSIONS

The combination of high-resolution XES-XAS spectroscopies applied to the study of the different magneto-electrical phases in $\text{Nd}_{0.5}\text{Sr}_{0.5}\text{MnO}_3$ has provided valuable information on the electronic state and local geometry of the Mn atom. Several works were reported earlier on XES experiments in perovskite manganites [8,48,50,51,58,60,62] but they were limited to only one de-excitation channel (mainly Mn CTC $K\beta$ XES) and lack exhaustive temperature dependence. Conversely, our XES study includes the Mn $K\alpha$ and $K\beta$ emission lines and in the latter both the CTC ($K\beta_{1,3}$ and $K\beta'$ lines) and VTC ($K\beta_{2,5}$ and $K\beta''$ lines) regions as a function of temperature. We obtain that the Mn $K\beta$ XES spectra are almost identical in the paramagnetic, metallic-ferromagnetic, and CO phases of $\text{Nd}_{0.5}\text{Sr}_{0.5}\text{MnO}_3$. This finding indicates that the Mn oxidation and spin state are not significantly changed by the different magnetic and electrical behavior. Only modest variations are observed accompanying the passage to the ferromagnetic-metallic phase when looking at the thermal difference signals of the Mn CTC $K\beta$ spectra, which are reversed when entering the charge-ordered one. These changes agree with a small decrease of the local spin density in the ferromagnetic-metallic phase compared with the paramagnetic and antiferromagnetic insulating phases. The absence of major changes seems to be controversial in regards to the CO phase of $\text{Nd}_{0.5}\text{Sr}_{0.5}\text{MnO}_3$ where there are two different Mn sites (conventionally described as Mn^{3+} and Mn^{4+} within a simple

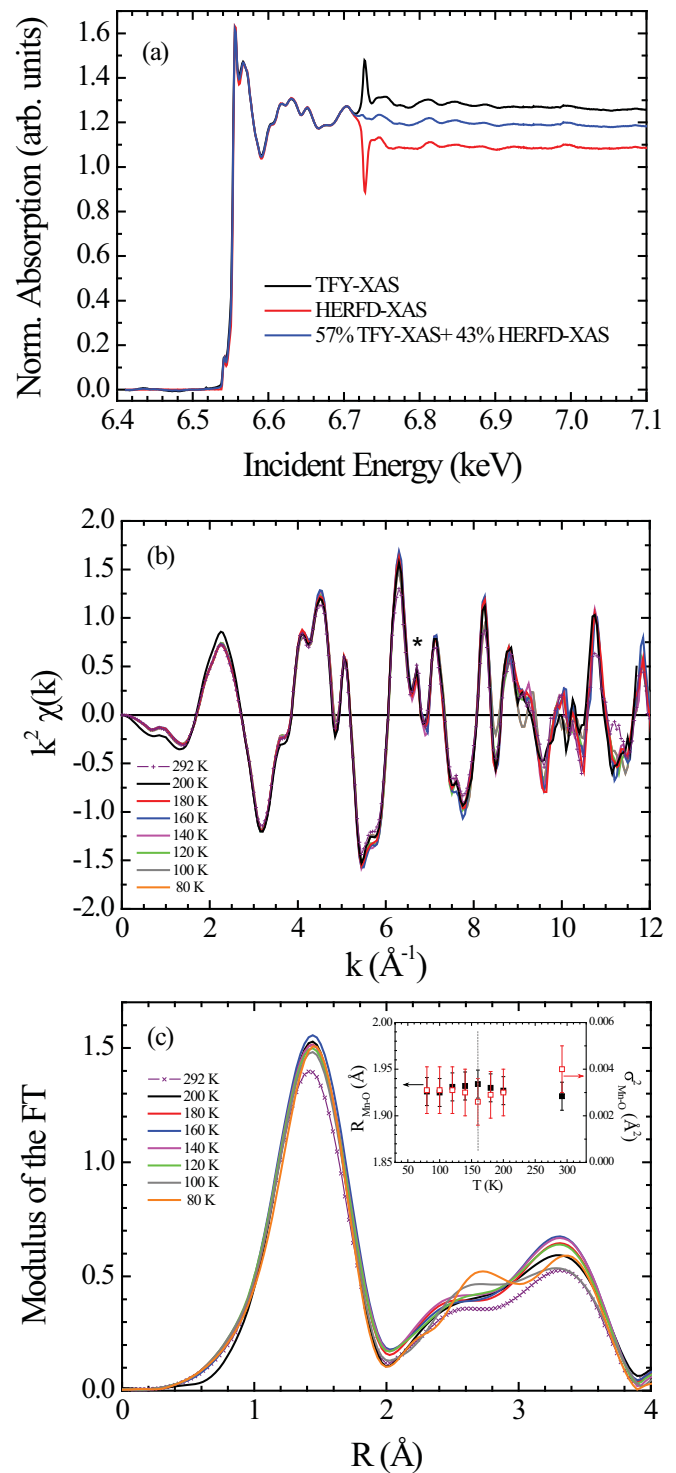


FIG. 7. EXAFS data of $\text{Nd}_{0.5}\text{Sr}_{0.5}\text{MnO}_3$. (a) Comparison between the HERFD-EXAFS at the Mn $K\alpha_1$, TFY-EXAFS and derived corrected EXAFS spectrum as described in the text. (b) $k^2 \chi(k)$ EXAFS signals between 292 K and 80 K. Asterisk indicates the position of the Nd L_2 edge white line. (c) Moduli of the FTs of the same signals. Inset: Temperature dependence of the refined Mn-O distance (closed squares, left axis) and Debye-Waller factor (open squares, right axis) derived from EXAFS data of $\text{Nd}_{0.5}\text{Sr}_{0.5}\text{MnO}_3$. The dashed line indicates the onset of the ferromagnetic-metallic to antiferromagnetic-CO transition.

ionic picture). We argue that the electronic difference among the two sites is too small to be detected or, in other words, the charge segregation between the two Mn sites is very small and hence the two sites are very similar. The largest differences in the Mn $K\alpha$ and $K\beta$ XES data have been observed across the different compounds (mixed-valent $\text{Nd}_{0.5}\text{Sr}_{0.5}\text{MnO}_3$ and single-valent NdMnO_3 , Sr/CaMnO_3). In all cases, the spectra of the single-valent samples can be grouped in two according to the Mn formal valence (Mn^{3+} and Mn^{4+}) while the spectra of $\text{Nd}_{0.5}\text{Sr}_{0.5}\text{MnO}_3$ show an intermediate behavior. Both the Mn $K\alpha_1$ FWHM and Mn $K\beta_{1,3}$ and $K\beta'$ lines position and intensity ratio depend on the local spin. Our results indicate that the spin value is in agreement with the mixed-valent state of the Mn atom intrinsic to half-doped $\text{Nd}_{0.5}\text{Sr}_{0.5}\text{MnO}_3$.

We now proceed to the discussion of the HERFD-XANES spectra, where we analyze the main edge and the prepeak structure separately. As noted in related works [6,8,9,22–25,47], the energy position of the main edge is correlated with the formal valence state of the Mn atom. In a first approximation, based on an ionic model, it can be stated that Mn in $\text{Nd}_{0.5}\text{Sr}_{0.5}\text{MnO}_3$ is composed by 50% Mn^{3+} and 50% Mn^{4+} , which would correspond to a formal valence 3.5+. If this were the case, then the HERFD-XANES should agree with the 1:1 addition of the spectra of NdMnO_3 and SrMnO_3 . This is justified by the fact that the main difference between XANES spectra of compounds with similar local structure geometry but different formal valence states comes from the energy shift of the main edge while the spectral shape remains largely unchanged [56]. However, we find that the HERFD-XANES spectrum of $\text{Nd}_{0.5}\text{Sr}_{0.5}\text{MnO}_3$ strongly disagrees with the 1:1 linear superposition of NdMnO_3 and SrMnO_3 spectra keeping their original chemical shift $\Delta E = 3.1$ eV as shown in Fig. 8. Since the interaction time for the K edge photoabsorption process is about 10^{-15} s, this finding means that there is neither spatial nor temporal distribution of purely ionic states Mn^{3+} and Mn^{4+} . This result seems to be at odds with the conventional description of the so-called CO phase at low temperatures in

terms of a $\text{Mn}^{3+}/\text{Mn}^{4+}$ bimodal distribution. X-ray diffraction and RXS experiments have reported a checkerboard ordering in the CO phase with two different Mn sites and noninteger valence states $\text{Mn}^{(3.5\pm\delta/2)+}$ where $\delta = 0.16 \pm 0.02$ [5]. The latter corresponds to $\Delta E = 0.6$ eV as follows from the linear relationship empirically found between chemical shift and charge segregation [56]. In Fig. 8 two more simulations of the $\text{Nd}_{0.5}\text{Sr}_{0.5}\text{MnO}_3$ spectrum in terms of 1:1 additions have been carried out taking into account this chemical shift value, either using the NdMnO_3 and SrMnO_3 spectra ($\text{Mn}^{3+}/\text{Mn}^{4+}$) or adding up the $\text{Nd}_{0.5}\text{Sr}_{0.5}\text{MnO}_3$ spectrum after applying shifts of $\pm\Delta E/2 = 0.3$ eV ($\text{Mn}^{3.42+}/\text{Mn}^{3.58+}$). The latter simulation fits nicely the HERFD-XANES of $\text{Nd}_{0.5}\text{Sr}_{0.5}\text{MnO}_3$ confirming in this way that in the CO phase the charge segregation is very small between the two different Mn sites, which are in intermediate valence states $\text{Mn}^{(3.5\pm\delta/2)+}$ as obtained in RXS experiments. Moreover, it is well known that the white line width increases with the lattice distortions [52]. We note that for NdMnO_3 where the local structure is tetragonal distorted, the white line width is larger than that of the Sr/CaMnO_3 compounds with regular structure. For $\text{Nd}_{0.5}\text{Sr}_{0.5}\text{MnO}_3$ it is similar to Sr/CaMnO_3 , indicating that the Mn atom is surrounded by an almost regular oxygen octahedron. This result is consistent with the lack of pure ionic Mn^{3+} and Mn^{4+} valences and corroborates the presence of Mn intermediate valence states with very small charge disproportionation. On the other hand, the spin-selective XANES spectra measured at the $K\beta_{1,3}$ and $K\beta'$ lines are shifted in energy by about 0.8 ± 0.2 eV for the four samples as deduced from the maximum of the derivatives. This shift arises from the exchange splitting whereby the spin-up states have lower energy than the spin-down states [59], being nearly independent of the Mn formal valence state.

The evolution obtained in the prepeak structures is more difficult to interpret. On one hand, the prepeaks have been associated to $1s \rightarrow 3d$ quadrupole transitions. However, the low intensity predicted for the quadrupole channel indicates that its contribution is very limited. A dipolar contribution to the prepeaks has been proposed due to the strong hybridization of Mn $4p$ orbitals with d orbitals of adjacent Mn atoms through the oxygen $2p$ orbitals by Elfimov *et al.* [65] in LaMnO_3 and Joly *et al.* [66] in TiO_2 . Overall, it seems that the pre-edge features contain information on the hybridization with the surrounding atoms and the splitting of the empty Mn d band. As follows from our results [see inset of Fig. 5(b)], the total intensity of the prepeaks increase with the Mn formal valence which can be interpreted as due to the enhancement of the $3d-2p-3d$ covalence (Mn–O–Mn) when going from Mn^{3+} - NdMnO_3 to Mn^{4+} - Sr/CaMnO_3 . In line with the XES results, the HERFD-XANES data do not show large variations with temperature. However, the difference spectra of the HERFD-XANES measured at the $K\alpha_1$ line reveal changes in the pre-edge region of mixed-valent $\text{Nd}_{0.5}\text{Sr}_{0.5}\text{MnO}_3$ (see Fig. 6) that reflect an increase of the $p-d$ hybridization in the ferromagnetic-metallic phase. This result nicely connects with the reduction in the local spin density deduced from the Mn CTC $K\beta$ XES spectra. Figure 9 shows the temperature dependence in the prepeak region of the spin-selective XANES measured at the $K\beta_{1,3}$ (spin-down) and $K\beta'$ (spin-up) lines at 300, 200, and 80 K for all the compounds. We first point out that there is no temperature dependence

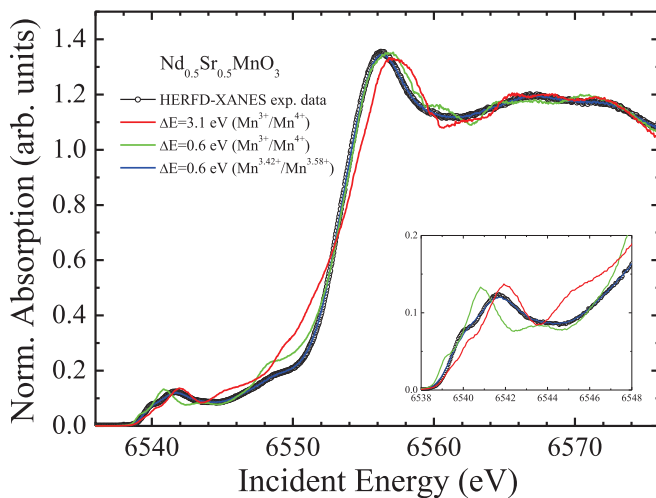


FIG. 8. HERFD-XANES at the Mn $K\alpha_1$ line of $\text{Nd}_{0.5}\text{Sr}_{0.5}\text{MnO}_3$ at RT compared with simulations based on 1:1 superpositions of different reference spectra and ΔE values as described in the text. Inset: Expansion of the pre-edge region.

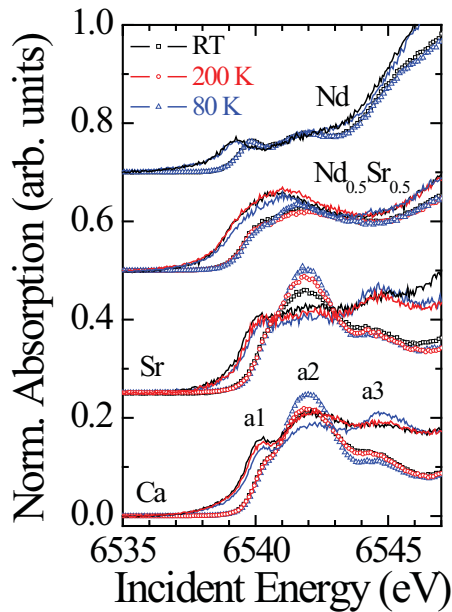


FIG. 9. Expansion of the pre-edge region of the temperature-dependent spin-selective XANES spectra measured at the Mn $K\beta_{1,3}$ (spin-down, solid lines) and $K\beta'$ (spin-up, open symbols) lines for $\text{Nd}_{0.5}\text{Sr}_{0.5}\text{MnO}_3$, NdMnO_3 , SrMnO_3 , and CaMnO_3 .

of the pre-edge spin-selective XANES for NdMnO_3 down to 80 K. This result can be expected because in the studied temperature range NdMnO_3 remains paramagnetic-insulator ($T_N \approx 78$ K) [38] and thus no changes are predicted in the valence, spin, or covalency of the Mn atoms. Nevertheless, a significant temperature and spin dependence of the pre-edge spectra is observed for $\text{Nd}_{0.5}\text{Sr}_{0.5}\text{MnO}_3$ and Sr/CaMnO_3 . In $\text{Nd}_{0.5}\text{Sr}_{0.5}\text{MnO}_3$ ($T_C \approx 250$ K and $T_N \approx 150$ K) upon cooling from room temperature to 200 K the a2 peak intensity is slightly reduced for the spin-down channel, whereas a strong enhancement of this intensity occurs with further cooling down to 80 K. A distinct decrease of the intensity of the a1 peak is also observed on cooling from 200 K to 80 K, primarily in the spin-up channel. A similar temperature variation of the pre-edge structure has been found in $\text{La}_{0.5}\text{Ca}_{0.5}\text{MnO}_3$ when entering the antiferromagnetic CO phase [60]. In the Mn^{4+} -compounds studied, similar changes are found when crossing T_N . Let us focus in the following on CaMnO_3 ($T_N \approx 125$ K [39]) as representative example. In the spin-up channel below 80 K, the a2 peak intensity increases while the a3 peak intensity decreases. In the spin-down channel the temperature dependence of these pre-edge structures is reversed below 80 K. Similar trends are seen for SrMnO_3 ($T_N \approx 230$ – 260 K [40–41]), but in this case the changes in temperature occur between room temperature and 200 K in agreement with the higher T_N . We can then conclude that the main changes in the electronic state of Mn atoms across the different magnetoelectrical phases are related to changes in the Mn $3d$ -O $2p$ covalency that are also intimately connected with changes in the magnetic ordering.

The EXAFS results on $\text{Nd}_{0.5}\text{Sr}_{0.5}\text{MnO}_3$ have shown that the Mn atom is surrounded by six O atoms at the same distance. The Mn-O interatomic distance is slightly larger at

the onset of the ferromagnetic-metallic phase, coincident with a minimum of the D-W [see Fig. 7(c)]. As previously reported for the $\text{La}_{1-x}\text{Ca}_x\text{MnO}_3$ series [9], in $\text{Nd}_{0.5}\text{Sr}_{0.5}\text{MnO}_3$ the MnO_6 octahedra are dynamically distorted in the paramagnetic high-temperature phase. With decreasing temperature, the system tends to stabilize by decreasing the local distortion due to the presence of long-range ferromagnetic interactions. But, below 170 K, when entering the statically ordered CO phase, this local distortion increases again and becomes temperature independent instead of collapsing as occurs for the magnetoresistive manganites [22,31]. To the general behavior of half-doped manganites, our EXAFS results in $\text{Nd}_{0.5}\text{Sr}_{0.5}\text{MnO}_3$ add the finding that the local structural differences at the Mn atom between the ferromagnetic-metallic and CO phases are also very small.

In summary, this XAS-XES study performed in $\text{Nd}_{0.5}\text{Sr}_{0.5}\text{MnO}_3$, where the three characteristic phases of the hole-doped manganites are present in separated temperature ranges, demonstrates that the local structure and the electronic state at the Mn atom hardly change among the different phases. However, they clearly differ between the half-doped system and the single-valent Mn^{3+} and Mn^{4+} parent compounds. In this way, the appearance of ferromagnetic-metallic and antiferromagnetic-CO phases must arise from the reported very small differences. Similarly, Fe $K\alpha$ and $K\beta$ XES measurements reported no differences across the metal-insulator transition in Fe_3O_4 , the archetypal CO system [67]. These results impose serious constraints on the theoretical models used to describe the mechanisms responsible for the appearance of magnetoresistance and CO phenomena. Conventionally, the theoretical models that describe the behavior of half-doped manganites adopted the ionic picture following the pioneer work of Goodenough *et al.* [68,69]. The latter considers the existence of Mn^{3+} and Mn^{4+} ions temporally separated but randomly distributed in the lattice for the paramagnetic-insulator and ferromagnetic-metallic phases and spatially ordered Mn^{3+} and Mn^{4+} ions in a checkerboard arrangement for the CO phase. This simple model has been already questioned by experimental XAS [5,6,8,9,22,23], RXS [27–30], and bond valence sum analysis [70,71] results showing that the Mn electronic and local structure in the mixed-valent compounds cannot be explained in terms of single-valent integer states. In the so-called CO phases, the charge disproportionation between the distinct Mn sites is nearly indiscernible. Most of the models are based on the uniformity of the doping and take as a basis the description of the electronic states of the Mn atom in an octahedral crystal field. It is, however, crucial to note that the structure is not periodic in the doped oxides. The divalent metal and the rare-earth atoms are randomly distributed in such a way that the crystal field at each of the Mn atoms, and also the local valence, change from site to site. For example, in $\text{Nd}_{0.5}\text{Sr}_{0.5}\text{MnO}_3$ the Mn atoms can be surrounded by any combination of $(8-n)$ Nd + n Sr neighbors. It has been experimentally demonstrated that the properties of divalent metal rare-earth ordered compounds show a markedly different behavior compared with the disordered ones [72,73]. The key point is that the electronic state at the Mn atom is uniform across the crystal, demonstrating that a strong electronic mixing occurs in the solid. Therefore, the Mn electronic state at each site corresponds to the geometrical average.

Recently, the Wannier states theory [7] was applied to resolve the apparent contradiction between the observed weak charge disproportionation and the traditional $\text{Mn}^{3+}/\text{Mn}^{4+}$ ionic picture of the charge-orbital order in half-doped manganites. The doped holes are found to reside primarily in the oxygen atoms forming a hybrid Wannier orbital of Mn e_g symmetry. Within this effective Mn e_g basis, a large difference in the d occupation numbers of the Mn Wannier molecular states is obtained according to the conventional $\text{Mn}^{3+}/\text{Mn}^{4+}$ ionic picture. However, due to the similar degree of mixing among the intrinsic Mn orbitals, the calculated difference between the localized charge at the Mn atoms is very weak in agreement with the experimentally observed charge disproportionation. We note that this Wannier states analysis does not really solve the contradiction. The problem is that it calculates a very small charge difference between the two end members (single-valent Mn^{3+} and Mn^{4+} parent compounds) which is similar to the predicted charge disproportionation for the half-doped compound [7]. This means that the two Mn sites in the half-doped system correlate quite well with the Mn electronic state of the Mn^{3+} and Mn^{4+} compounds. On the contrary, the charge determined from experiments using XAS and/or RXS techniques results from the assumption that the valences 3+ and 4+ correspond to zero-hole and one-hole doping. That is, the charge disproportionation in the half doped sample is 5 times smaller than the charge difference between the single-valent parent compounds. In any case, we think that a band model similar to that of Refs. [7,11] with

strong delocalization of the Mn d states will describe better the experimental facts than the conventional ionic model.

Finally, the similarity of the Mn local structural and electronic state at the different magnetoelectrical phases also explains the strong competition between the ferromagnetic-metallic and the CO phases and the strong sensitivity of the latter to external conditions such as magnetic field [21,74], electric field [75], or photon illumination [76,77]. Moreover, this competition could also be responsible for the phase separation phenomenon in manganites [77] used to explain the magnetoresistance effect. This finding imposes serious questions concerning the mechanisms that govern the appearance of each phase. In conclusion, theoretical studies must take into account the weak electronic and structural evolution at the Mn sites with temperature and the strong delocalization of the Mn d states in order to provide a realistic interpretation of the magnetoresistance and CO phenomena.

ACKNOWLEDGMENTS

The authors thank ESRF for granting beam time and ID26 beamline staff for their assistance during the experiments. We also thank V. Cuartero for the conventional XAS measurements. Finally, we acknowledge financial support from the Spanish MINECO (Project No. MAT2015-68760-C2-1, cofunded by ERDF from EU) and Diputación General de Aragón (DGA-CAMRADS).

-
- [1] J. M. D. Coey, M. Viret, and S. Molnar, *Adv. Phys.* **48**, 167 (1999).
- [2] E. Dagotto, T. Hotta, and A. Moreo, *Phys. Rep.* **344**, 1 (2001).
- [3] S.-W. Cheong and H. Y. Hwang, in *Contribution to Colossal Magnetoresistance Oxides, Monographs in Condensed Matter Science*, edited by Y. Tokura (Gordon & Breach, London, 1999).
- [4] Y. Tokura, *Rep. Prog. Phys.* **69**, 797 (2006), and references therein.
- [5] J. Herrero-Martin, J. García, G. Subías, J. Blasco, and M. C. Sánchez, *Phys. Rev. B* **70**, 024408 (2004).
- [6] G. Subías, J. García, M. G. Proietti, and J. Blasco, *Phys. Rev. B* **56**, 8183 (1997).
- [7] D. Volja, W.-G. Yin, and W. Ku, *Europhys. Lett.* **89**, 27008 (2010).
- [8] T. A. Tyson, Q. Qian, C. C. Kao, J. P. Rueff, F. M. F. de Groot, M. Croft, S.-W. Cheong, M. Greenblatt, and M. A. Subramanian, *Phys. Rev. B* **60**, 4665 (1999).
- [9] J. García, M. C. Sanchez, G. Subías, and J. Blasco, *J. Phys.: Condens. Matter*, **13**, 3229 (2001).
- [10] K. J. Thomas, J. P. Hill, S. Grenier, Y.-J. Kim, P. Abbamonte, L. Venema, A. Rusydi, Y. Tomioka, Y. Tokura, D. F. McMorrow, G. Sawatzky, and M. van Veenendaal, *Phys. Rev. Lett.* **92**, 237204 (2004).
- [11] V. Ferrari, M. Towler, and P. B. Littlewood, *Phys. Rev. Lett.* **91**, 227202 (2003).
- [12] Y. Tomioka, A. Asamitsu, H. Kuwahara, Y. Moritomo, and Y. Tokura, *Phys. Rev. B* **53**, R1689 (1996).
- [13] Y. Tokura, H. Kuwahara, Y. Moritomo, Y. Tomioka, and A. Asamitsu, *Phys. Rev. Lett.* **76**, 3184 (1996).
- [14] P. G. Radaelli, M. Marezio, H. Y. Hwang, S.-W. Cheong, and B. Batlogg, *Phys. Rev. Lett.* **75**, 4488 (1995).
- [15] P. G. Radaelli, D. E. Cox, M. Marezio, and S.-W. Cheong, *Phys. Rev. B* **55**, 3015 (1997).
- [16] B. J. Sternlieb, J. P. Hill, U. C. Wildgruber, G. Luke, B. Nachumi, Y. Moritomo, and Y. Tokura, *Phys. Rev. Lett.* **76**, 2169 (1996).
- [17] Y. Moritomo, Y. Tomioka, A. Asamitsu, Y. Tokura, and Y. Matsui, *Phys. Rev. B* **51**, 3297 (1995).
- [18] Y. Wakabayashi, Y. Murakami, I. Koyama, T. Kimura, Y. Tokura, Y. Moritomo, K. Hirota, and Y. Endoh, *J. Phys. Soc. Jpn.* **69**, 2731 (1999).
- [19] C. H. Chen, S.-W. Cheong, and H. Y. Hwang, *J. Appl. Phys.* **81**, 4326 (1997).
- [20] S. Mori, C. H. Chen, and S.-W. Cheong, *Phys. Rev. Lett.* **81**, 3972 (1998).
- [21] H. Kuwahara, Y. Tomioka, A. Asamitsu, Y. Moritomo, and Y. Tokura, *Science* **270**, 961 (1995).
- [22] C. H. Booth, F. Bridges, G. H. Kwei, J. M. Lawrence, A. L. Cornelius, and J. Neumeier, *Phys. Rev. B* **57**, 10440 (1998).
- [23] M. Croft, D. Sillis, M. Greenblatt, C. Lee, S.-W. Cheong, K.-V. Ramanujachary, and D. Tran, *Phys. Rev. B* **55**, 8726 (1997).
- [24] R. S. Liu, J. B. Wu, C. Y. Chang, J. G. Lin, C. Y. Huang, J. M. Chen, and R. G. Liu, *J. Solid State Chem.* **125**, 112 (1996).
- [25] E. Pellegrin, L. H. Tjeng, F. M. F. de Groot, R. Hesper, G. A. Sawatzky, Y. Moritomo, and Y. Tokura, *J. Electron Spectrosc. Relat. Phenom.* **86**, 115 (1997).
- [26] J. García, M. C. Sanchez, J. Blasco, G. Subías, and M. G. Proietti, *J. Phys.: Condens. Matter* **13**, 3243 (2001).

- [27] S. Di Matteo, T. Chatterji, Y. Joly, A. Stunault, J. A. Paixao, R. Suryanarayanan, G. Dhalenne, and A. Revcolevschi, *Phys. Rev. B* **68**, 024414 (2003).
- [28] S. Grenier, J. P. Hill, D. Gibbs, K. J. Thomas, M. V. Zimmerman, C. S. Nelson, V. Kiryukhin, Y. Tohura, Y. Tomioka, D. Casa, T. Gog, and C. Venkataraman, *Phys. Rev. B* **69**, 134419 (2004).
- [29] G. Subías, J. García, P. Beran, M. Nevriwa, M. C. Sanchez, and J. L. García-Munoz, *Phys. Rev. B* **73**, 205107 (2006).
- [30] J. Herrero-Martín, J. Blasco, J. García, G. Subías, and C. Mazzoli, *Phys. Rev. B* **83**, 184101 (2011).
- [31] G. Subías, J. García, J. Blasco, and M. G. Proietti, *Phys. Rev. B* **57**, 748 (1998).
- [32] F. Bridges, L. Downward, J. J. Neumeier, and T. A. Tyson, *Phys. Rev. B* **81**, 184401 (2010).
- [33] G. Subías, J. García, J. Blasco, M. C. Sánchez, and M. G. Proietti, *J. Phys. Condensed Matter* **14**, 5017 (2002).
- [34] G. Peng, F. M. F. de Groot, K. Hämäläinen, J. A. Moore, X. Wang, M. M. Grush, J. B. Hastings, D. P. Siddons, W. H. Armstrong, O. C. Mullins, and S. P. Cramer, *J. Am. Chem. Soc.* **116**, 2914 (1994).
- [35] P. Glatzel and U. Bergmann, *Coord. Chem. Rev.* **249**, 65 (2005).
- [36] M. Rovezzi and P. Glatzel, *Semicond. Sci. Technol.* **29**, 023002 (2014).
- [37] K. Hämäläinen, D. P. Siddons, J. B. Hastings, and L. E. Berman, *Phys. Rev. Lett.* **67**, 2850 (1991).
- [38] A. Muñoz, J. A. Alonso, M. J. Martínez-Lope, J. L. García-Muñoz, and M. T. Fernández-Díaz, *J. Phys. Condens. Matter* **12**, 1361 (2000).
- [39] Z. Zeng, M. Greenblatt, and M. Croft, *Phys. Rev. B* **59**, 8784 (1999).
- [40] T. Takeda and S. Ohara, *J. Phys. Soc. Jpn.* **37**, 275 (1974).
- [41] O. Chmaissem, B. Dabrowski, S. Kolesnik, J. Mais, D. E. Brown, R. Kruk, P. Prior, B. Pyles, and J. D. Jorgensen, *Phys. Rev. B* **64**, 134412 (2001).
- [42] J. M. de Teresa, J. Blasco, M. R. Ibarra, J. García, C. Marquina, P. Algarabel, and A. del Moral, *Solid State Commun.* **96**, 627 (1995).
- [43] M. R. Ibarra, P. A. Algarabel, C. Marquina, J. Blasco, and J. García, *Phys. Rev. Lett.* **75**, 3541 (1995).
- [44] C. Suzuki, J. Kawai, J.-y. Tanizawa, H. Adachi, S. Kawasaki, M. Takano, and T. Mukoyama, *Chem. Phys.* **241**, 17 (1999).
- [45] E. Gallo and P. Glatzel, *Adv. Mater.* **26**, 7730 (2014).
- [46] D. C. Koningsberger and R. Prins, *X-ray Absorption: Principles, Applications, Techniques of EXAFS, SEXAFS and XANES* (Wiley, New York, 1988).
- [47] J. J. Rehr and R. C. Albers, *Rev. Mod. Phys.* **72**, 621 (2000).
- [48] B. Ravel and M. Newville, *J. Synchrotron Rad.* **12**, 537 (2005).
- [49] G. Vankó, T. Neisius, G. Molnar, F. Renz, S. Kárpáti, A. Shukla, and F. M. F. De Groot, *J. Phys. Chem.* **110**, 11647 (2006).
- [50] Q. Qian, T. A. Tyson, C.-C. Kao, M. Croft, S.-W. Cheong, and M. Greenblatt, *Phys. Rev. B* **62**, 13472 (2000).
- [51] J. Herrero-Martín, A. Mirone, J. Fernández-Rodríguez, P. Glatzel, J. García, J. Blasco, and J. Geck, *Phys. Rev. B* **82**, 075112 (2010).
- [52] J. A. Alonso, M. J. Martínez-Lope, and M. T. Casais, *Inorg. Chem.* **39**, 917 (2000).
- [53] P. D. Battle, T. C. Gibb, and C. W. Jones, *J. Solid State Chem.* **74**, 60 (1988).
- [54] J. Blasco, C. Ritter, J. García, J. M. de Teresa, J. Pérez-Cacho, and M. R. Ibarra, *Phys. Rev. B* **62**, 5609 (2000).
- [55] U. Bergmann, C. R. Horne, T. J. Collins, J. M. Workman, and S. P. Cramer, *Chem. Phys. Lett.* **302**, 119 (1999).
- [56] J. Garcia, G. Subias, V. Cuartero, and J. Herrero-Martín. *J. Synch. Rad.* **17**, 386 (2010).
- [57] X. Wang, F. M. F. deGroot, and S. P. Cramer, *Phys. Rev. B* **56**, 4553 (1997).
- [58] H. Hayashi, A. Sato, T. Azumi, Y. Udagawa, T. Inami, K. Ishii and K. B. Garg, *Phys. Rev. B* **73**, 134405 (2006).
- [59] K. Hämäläinen, C.-C. Kao, J. B. Hastings, D. P. Siddons, L. E. Berman, V. Stojanoff, and S. P. Cramer, *Phys. Rev. B* **46**, 14274 (1992).
- [60] Q. Qian, T. A. Tyson, S. Savrasov, C.-C. Kao, and M. Croft, *Phys. Rev. B* **68**, 014429 (2003).
- [61] Q. Qian, T. A. Tyson, C.-C. Kao, M. Croft, and A. Yu. Ignatov, *Appl. Phys. Lett.* **80**, 3141 (2002).
- [62] Q. Qian, T. A. Tyson, C.-C. Kao, M. Croft, S.-W. Cheong, G. Popov, and M. Greenblatt, *Phys. Rev. B* **64**, 024430 (2001).
- [63] F. Bridges, C. H. Booth, M. Anderson, G. H. Kwei, J. J. Neumeier, J. Snyder, J. Mitchell, J. S. Gardner, and E. Brosha, *Phys. Rev. B* **63**, 214405 (2001).
- [64] M. Bianchini and P. Glatzel, *J. Synchr. Rad.* **19**, 911 (2012).
- [65] I. S. Elfimov, V. I. Anisimov, and G. A. Sawatzky, *Phys. Rev. Lett.* **82**, 4264 (1999).
- [66] Y. Joly, D. Cabaret, H. Renevier, and C. R. Natoli, *Phys. Rev. Lett.* **82**, 2398 (1999).
- [67] M. Wilcke, W. A. Caliebe, and P. Machek, *J. Phys. Conf. Series* **190**, 012090 (2009).
- [68] J. B. Goodenough, *Phys. Rev.* **100**, 564 (1955).
- [69] J. B. Goodenough, *Magnetism and the Chemical Bond* (Interscience, New York, 1963).
- [70] R. D. Shanon, *Acta Cryst. A* **32**, 751 (1976).
- [71] I. D. Brown, *Acta Cryst. B* **48**, 553 (1992).
- [72] D. Akahoshi, M. Uchida, Y. Tomioka, T. Arima, Y. Matsui, and Y. Tokura, *Phys. Rev. Lett.* **90**, 177203 (2003).
- [73] D. Akahoshi, Y. Okimoto, M. Kubota, R. Kumai, T. Arima, Y. Tomioka, and Y. Tokura, *Phys. Rev. B* **70**, 064418 (2004).
- [74] H. Kuwahara, Y. Moritomo, Y. Tomioka, A. Asamitsu, M. Kasai, and Y. Tokura, *J. Appl. Phys.* **81**, 4954 (1997).
- [75] A. Asamitsu, Y. Tomioka, H. Kuwahara, and Y. Tokura, *Nature* **388**, 50 (1997).
- [76] V. Kiryukin, D. Casa, J. P. Hill, B. Keimer, A. Vigilante, Y. Tomioka, and Y. Tokura, *Nature* **386**, 813 (1997).
- [77] P. G. Radaelli, M. Marezio, H. Y. Hwang, S.-W. Cheong, and B. Batlogg, *Phys. Rev. B* **54**, 8992 (1996).